"The Aerodynamics of Heavy Vehicles: Trucks, Busses and Trains",

Monterey-Pacific Grove, California, USA, 2002

Exploring the Flow Around a Simplified Bus with Large Eddy Simulation and Topological Tools

Siniša Krajnović[1] and Lars Davidson[2]

[1] Department of Thermo and Fluid Dynamics, Chalmers University of Technology, SE-41296 Göteborg, Sweden, sinisa@tfd.chalmers.se

[2] Department of Thermo and Fluid Dynamics, Chalmers University of Technology, SE-41296 Göteborg, Sweden, lada@tfd.chalmers.se

Abstract

The results of the large eddy simulation of the flow around a simplified bus presented in [11, 12] are used to describe this flow in detail. Using time-averaged trace lines on the surface of the body, the patterns of the shear-stress lines are revealed and used to identify bifurcation lines and critical points (zero-shear-stress points) in the flow. This information is then used to establish a complete picture of the flow on the surface of the body that can be used for understanding soiling and accumulation of water on the surface or in determinations of aeroacoustic noise sources. Kinematical investigations of the flow in two symmetry planes were done to reveal the critical points in the flow. With this it was proven that the flow resulting from numerical simulation is kinematically possible.

1 Introduction

Our success in predicting the behavior of the vehicle in the air stream is strongly dependent on our knowledge of the flow influencing the vehicle. The complexity of the structures in this three-dimensional flow makes experimental studies very difficult. Furthermore, experimental studies often provide only information on some limited partition of the flow (point, line or a plain). Computational fluid dynamics (CFD) gives a description of the flow in the entire computational domain (numerical wind tunnel). Unfortunately, the Reynolds-Averaged Navier-Stokes equation (RANS) commonly used in prediction of this

flow suppresses too much information. This method has also difficulty in predictions of the momentum transport after separation, which makes it difficult to rely on the prediction of separated flows.

Use of transient simulations such as unsteady RANS simulations (URANS) and large eddy simulations (LES) have proved to be successful in predicting flows with separations. URANS gives a flow field that represents the large-scale dynamics but that is smoother than the true field. This is a direct consequence of the strong influence of RANS modeling in URANS. Large eddy simulation gives rich information on the flow, but the LES of the flow around the full scale vehicle at the road condition is beyond the reach of today's computers [11], although computer power is increasing with giant steps. As an example we can compare the simulation presented in this paper, which required five months of computation on a million dollar parallel computer. The authors are now making the same size simulation in two weeks on a thirty thousand dollar Linux cluster. This computational effort can be compared with several days to one week of RANS simulation that is typical in the automotive industry. Although there have been great achievements in computational power, LES is best used in flows around vehicle models at lower Reynolds numbers, see [11]. Hybrid RANS/LES simulations [6, 5, 15] are probably more amenable for simulation of the flow at road conditions, and these are currently under development.

Extracting knowledge of the flow around vehicles from the flow at lower Reynolds number is not new and has been used for a long time in experimental studies [3, 1, 2, 8]. However, the new ingredient in our approach is a use of LES that results in more detailed picture of the flow than the experimental one. The current paper studied the topology both on the surface and in the symmetry plane of the body. These investigations can be compared with oil flow visualizations and PIV studies used in experimental studies. The purpose of the surface study is to highlight the complex interaction of the body with the surrounding flow. This analysis is intended to provide information that will aid in our understanding of soiling and accumulation of water on the surface. It can also be used in determinations of aeroacoustic noise sources and the influence of the coherent structures in the flow on the stability properties of the vehicle.

2 Large eddy simulation

LES was made of the flow around a bus-shaped body and compared with experiments in [7, 8]. This flow is similar to the flow around a real vehicle, and some knowledge of this kind of flow is available from previous experimental and numerical studies [3, 1, 2, 8, 9]. As the flow is characterized by a fairly high Reynolds number (0.21×10^6, based on the model height H and the incoming velocity), the resulting flow features and the character of the flow-

induced forces on the body should be similar to that in the flow around a full-scale vehicle.

The shape of the body is based on the Ahmed's body [1] and it is shown placed above the wind tunnel wall in Fig. 1. A computational domain with an

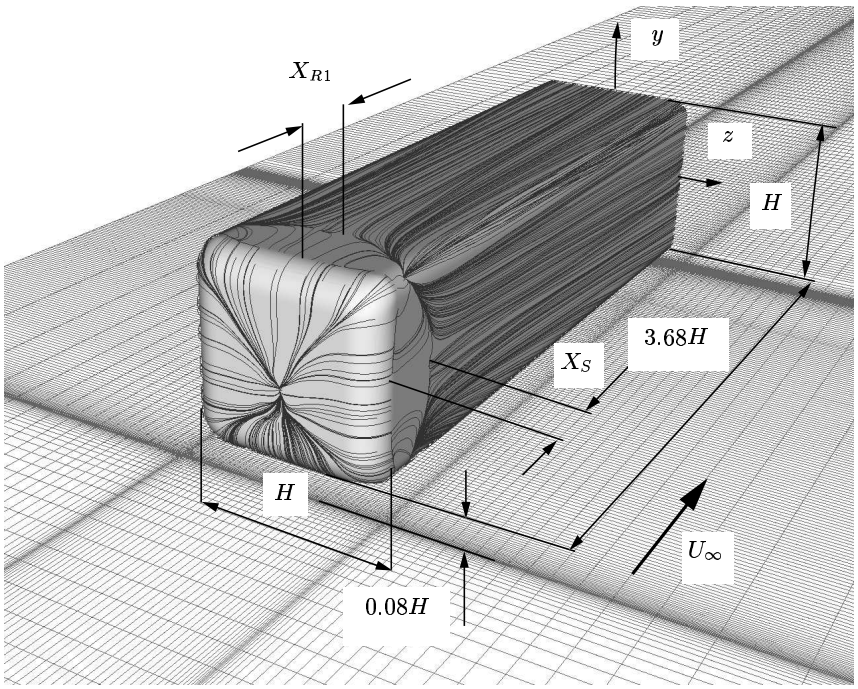

Fig. 1. Geometry of the bus-shaped body placed above the wind tunnel wall. Time-averaged trace lines are plotted on the surface of the body showing the roof and the lateral vortices that extend X_{R1} and X_S, respectively, in the stream-wise direction.

upstream length of $8H$, a downstream length of $21H$ and a span-wise width of $5.92H$ was used for the simulations. A moving ground belt in the experiment [7, 8] was simulated by applying the inlet velocity, U_∞, on the floor. The near-wall spatial resolution expressed in wall units was $\langle \Delta s^+ \rangle_t = 5 - 164$ in the stream-wise direction, $\langle \Delta n^+ \rangle_t = 0.5 - 0.8$ in the wall-normal direction and $\langle \Delta l^+ \rangle_t = 14 - 142$ in the span-wise direction. No-slip boundary conditions were applied on the solid walls. The Smagorinsky model [14] for the SGS stress tensor with Smagorinsky constant $C_S = 0.1$ was chosen for its simplicity and low computational cost.

3 Description of the flow topology

Time-averaged trace lines and streamlines are used to reveal critical points (i.e. points at which all the spatial derivative of the velocity are zero) and bifurcation lines in the flow. Critical points can be classified into three main groups: nodes, foci and saddles, of which nodes and foci can be stable and unstable. "Bifurcation lines are lines drawn in the flow toward which the trajectories are asymptotic"[13]. They are denoted negative bifurcation line (NBL) and positive bifurcation line (PBL), depending respectively on whether the trajectories approach or diverge the bifurcation line exponentially. These lines are associated with flow attachment (PBL) or separation (NBL). For a complete description of critical points and bifurcation lines, we refer to [13].

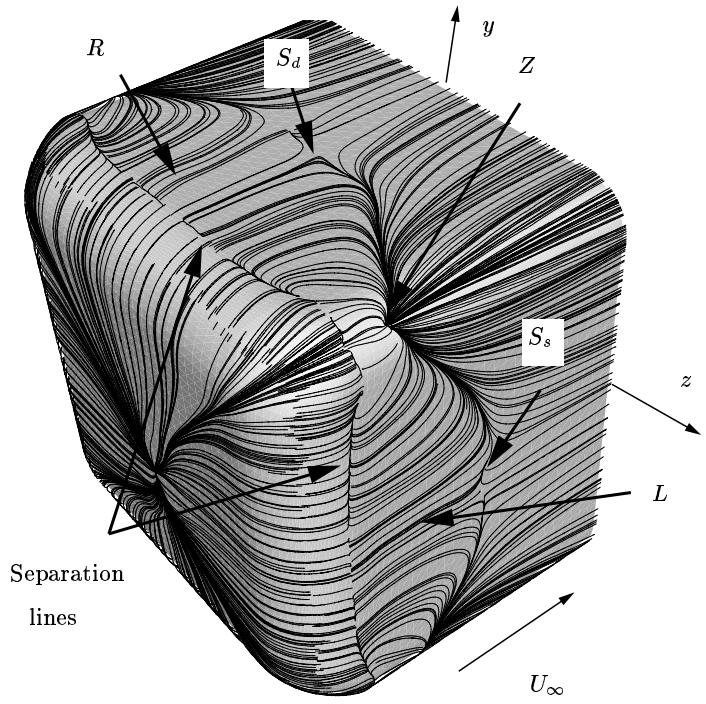

b)

Fig. 2. Time-averaged trace lines on the surface of the body showing the roof vortex, R, and the lateral vortex, L. View of the front face of the body.

Time-averaged trace lines, corresponding to oil flow visualization in experiments, are used to highlight the shear stresses lines on the body. At the front part of the body shown in Fig. 2, two kinds of critical points are visible. These are one unstable node Z (see also Fig. 3(a)) at the upper lateral edge of the bus and saddle points S_d (see also Fig. 3(b)) and S_s (see also Fig. 3(c))

downstream of separation regions R and L, respectively. Between these critical points several PBLs were observed (see Fig. 3), indicating the reattachment of the flow which separated at the leading edge upstream. Following these lines, beginning in the unstable node on the upper lateral corner, Z, the flow direction is toward the saddles. The flow on the surface upstream of the PBLs is opposite of the free-stream direction. This is the result of the interaction of the unstable node with the saddle points. As the unstable node works as the repeller of the flow in all four directions, the saddle point attracts the flow from the unstable node, only to repel it in the perpendicular direction, i.e. upstream and downstream. It is possible that the trace lines leaving node Z in the upstream direction toward the separation line end in a stable node in region Q in Fig. 3(a).

Similar to node Z, the unstable node G (see Fig. 4) is found close to the lower lateral corner of the body. The surface flow in this region is complex due to the presence of the stable focus F_c. The flow coming underneath the bus is deflected by this focus, and the fluid particle closest to it travels in spiral paths ending in the focus. At the same time the node is deflecting the flow. The partition of the flow that is deflected downstream forms together with the stream-wise flow on the underneath surface, the negative bifurcation line (NBL) shown in Fig. 5(a). This NBL indicates separation of the flow and results in lateral vortices (see [11, 12]). No bifurcation lines were observed on the upper lateral edge (see Fig. 5(b)).

Flow on the rear face of the bus is very complex. The shear stresses here are very low, making it difficult to represent the surface topology using trace lines. Thus the surface topology on the rear of the bus is not presented in this paper.

Besides the study of the surface topology, kinematical studies of the flow in two symmetry planes were conducted. This was done to identify the critical points in the flow and to determine whether the flow resulting from the simulation was kinematically possible.

The most common critical points on the border between the surface of the body and the surrounding flow are half-saddles (see Figs. 6 – 9). The half-saddle indicating the reattachment is always the mirror image of the half-saddle indicating the corresponding separation (see e.g. Fig. 8(c), where the reattachment point S_{13} is the mirror image of the separation point S_{12}). In the $x-y$ plane close to the front part of the body, three half-saddles, S_1, S_2 and S_3, were detected (see Fig. 6). In this figure, half-saddle S_1 represents the stagnation point and S_2 and S_3 indicate points of separation and reattachment, respectively, of the recirculation region on the roof of the bus (region R in Fig. 2). One stable focus, N_1, was also identified in the recirculation region (see Fig. 6).

As the flow separates at the rear of the bus, the region of recirculating flow, shown in Fig. 7, is formed. Two thin vortices B, shown in Fig. 7, are formed on the rear surface in the $x-y$ plane. Figures 7(b) and (c) show that the direction of rotation of the upper-edge and lower-edge vortices is counter-clockwise and

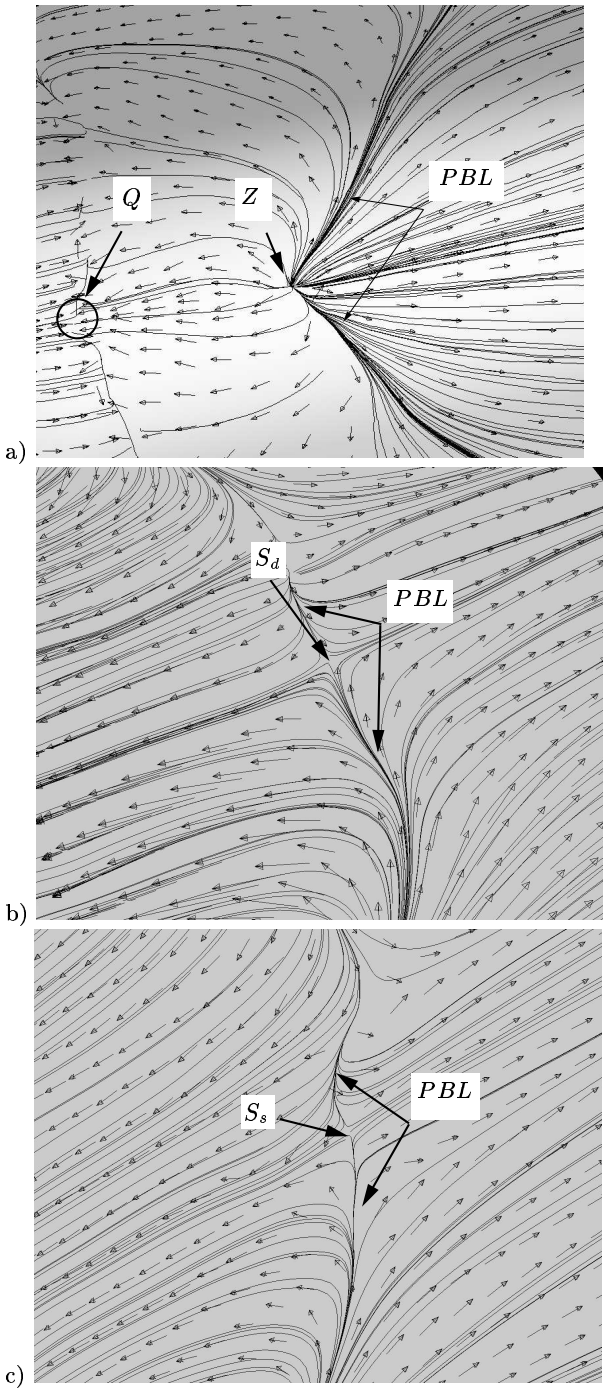

Fig. 3. Time-averaged trace lines on the surface of the body showing the unstable node, Z (a), and the saddle points, S_d (b) and S_s (c), downstream of the separation region, R and L, respectively. PBL are positive bifurcation lines, i.e. attachment lines. The velocity vectors are plotted at the surface parallel to the body surface at the wall-normal distance of $1.6 \times 10^{-4} H$.

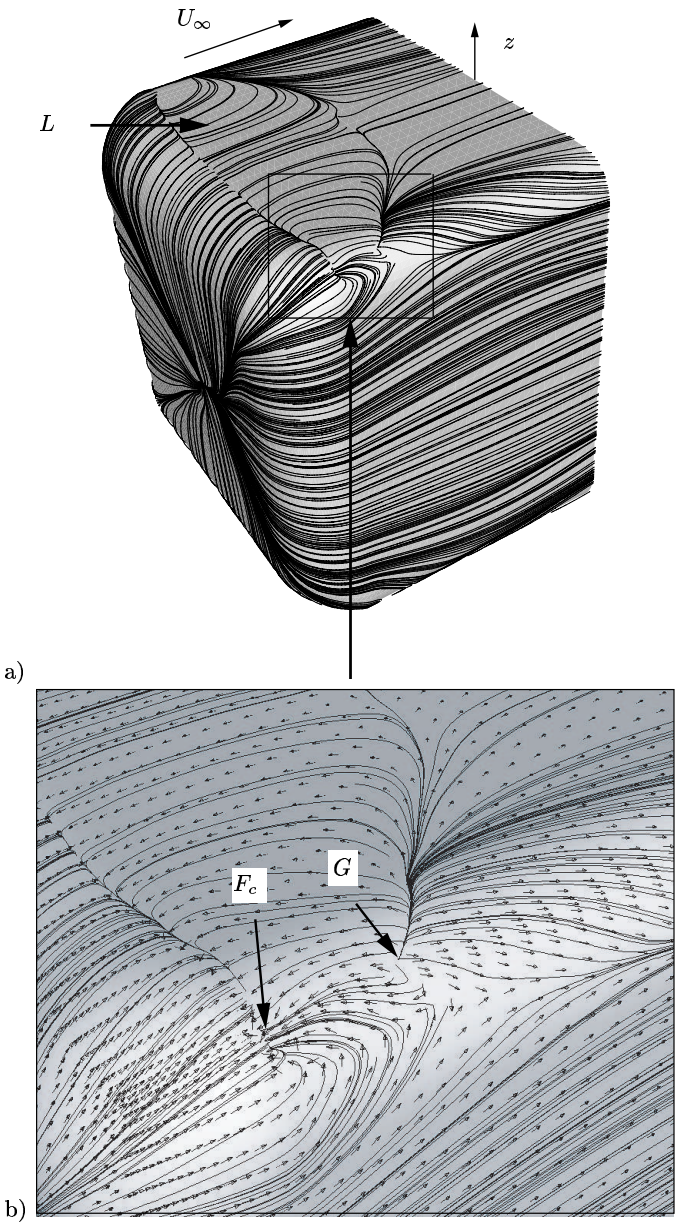

Fig. 4. a) Time-averaged trace lines on the surface of the body. View from below. b) Zoom of Fig. (a). The velocity vectors are plotted at the surface parallel to the body surface at wall-normal distance of $1.6 \times 10^{-4} H$. F_c is a focus and G is an unsteady node [13].

clockwise, respectively. Separations of the flow responsible for these structures are indicated with half-saddles S_6 and S_7 and reattachments with half-saddles S_5 and S_8 for lower-edge and upper-edge vortices, respectively (see Figs. 7(b) and 7(c)). It is interesting to note that both vortices B are fed with the flow pushed away by half-saddle S_{10} in the free stagnation point. One part of this flow coming from S_{10} passes vortices B and interacts with the separated flow in the x direction at $y = \pm H/2$ and forms half-saddles S_4 and S_9 close to the lower and upper edges of the bus, respectively. The main part of the recirculating region behind the bus consists of the counter-rotating vortices whose cores are represented in Fig. 7(a) with two stable foci, $F1$ and $F2$. Between these two vortices and the shear layer closing the recirculating region, an additional saddle, D, was found.

Similar to the description of the flow in the $x-y$ plane presented above, the flow in the $x-z$ plane can be described using Figs. 8 and 9. It was found in this plane that the incoming flow to the front part of the bus is divided into two equal parts which are then pushed away in the direction perpendicular to that of the incoming flow. A half-saddle S_{11} depicted in Figs. 8(a) and 8(b) indicates the presence of the stagnation point. As the flow separates after the rounded edges at the half-saddles S_{12} and S_{14}, two regions of recirculating flow are formed with their cores indicated with stable foci N_6 and N_7, respectively. Being detached a certain distance, this flow attaches again in half-saddles S_{13} and S_{15} (see Figs. 8(a) and 8(c)). The existence of these two recirculating regions in the $x-y$ plane compared to only one in the $x-z$ plane is the result of the symmetry in geometry (and thereby in flow) with respect to plane $y = 0$. In the $x-z$ plane, at the rear edge of the bus, the boundary layer also goes over into a shear layer surrounding two large vortices, of which one is shown in Fig. 9(a). These large counter-rotating vortices (see Fig. 11) have their center in stable foci N_{10} and N_{11}. Following the shear layer from the separation edge downstream, the fluid reaches saddle S_{23}. Similar to saddle D in the $x-y$ plane, saddle S_{23} is found to be connection between two vortices in the recirculating region and the surrounding flow in this plane. At saddle S_{23}, the shear layer is broken and the flow is deflected upstream and downstream. The result of the rotation of the vortices (with their foci N_{10} and N_{11}) is the impingement of the flow in the stagnation point depicted with half-saddle S_{21} in Fig. 11. From this point, the flow attached onto the rear of the bus is pushed away toward the lateral sides of the bus. Close to the lateral edges, this flow separates at half-saddles S_{18} and S_{19} and two thin vortices, B, are formed (see Fig. 9(b)). The center of these vortices is depicted in Figs. 9(b) and 11 with stable foci N_8 and N_9. These vortices extend to the point where the reattachments are depicted with half-saddles S_{16} and S_{20}. Again the attached flow meets the shear layer at $z = \pm H/2$, which deflects it in the stream-wise direction similar to what was found in the $x-y$ plane. This results in two half-saddles, S_{17} and S_{22}, shown in Figs. 9(b) and 11.

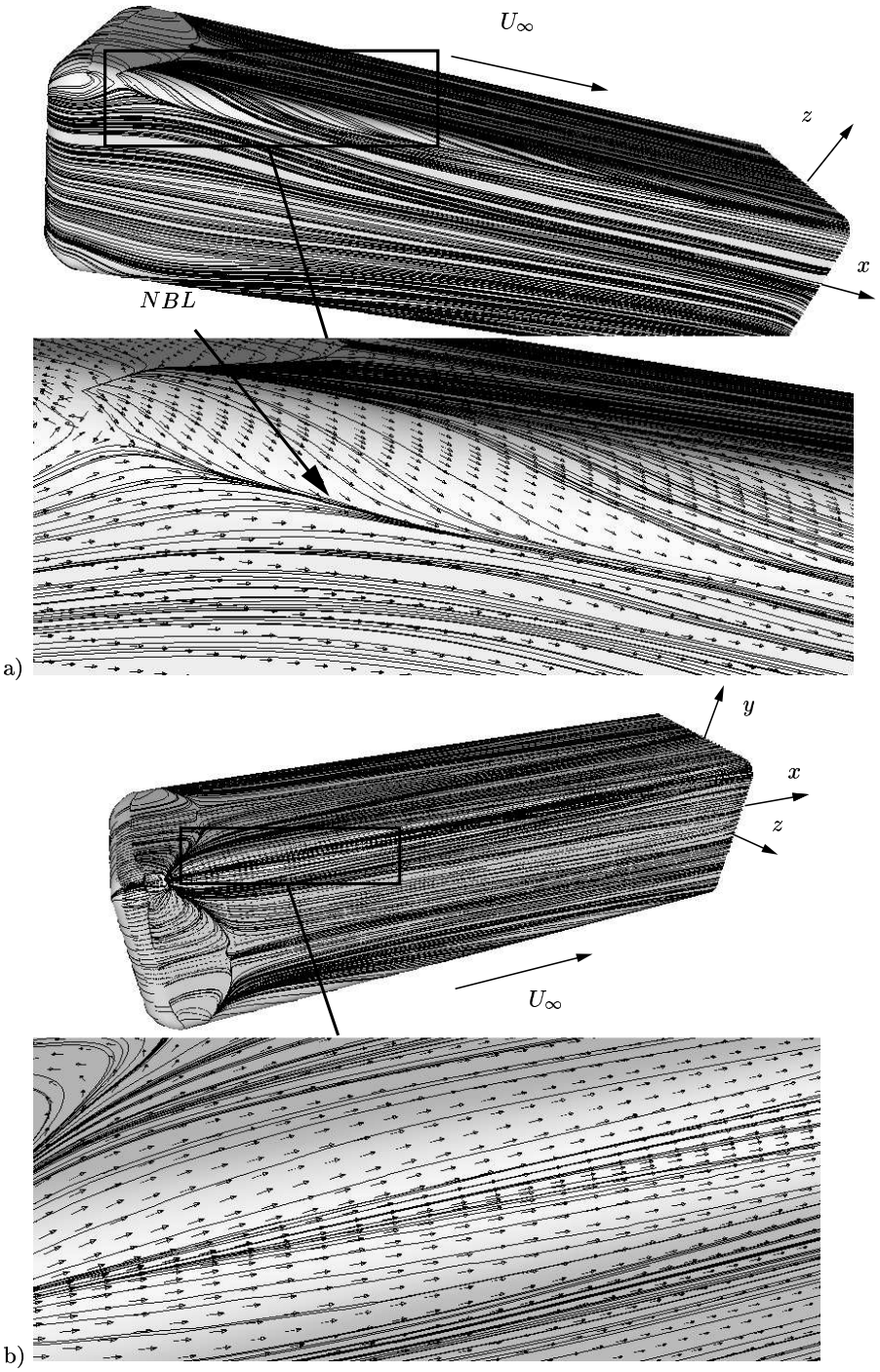

Fig. 5. Time-averaged trace lines on the surface of the body. a) View of the lower lateral edge. b) View of the upper lateral edge. NBL is the negative bifurcation line, i.e. the separation line. The velocity vectors are plotted at the surface parallel to the body surface at the wall-normal distance of $1.6 \times 10^{-4} H$.

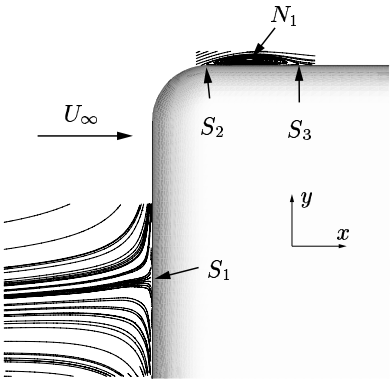

Fig. 6. Time-averaged streamlines projected onto symmetry plane $z = 0$ showing half-saddles S_1, S_2 and S_3 and focus N_1.

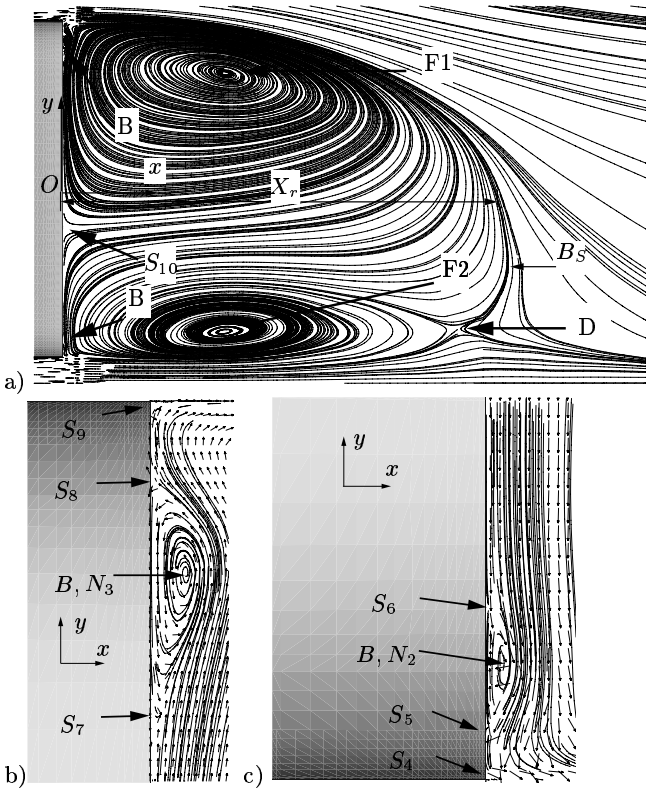

Fig. 7. a) Time-averaged streamlines projected onto symmetry plane $z = 0$ of the bus. S_{10} is the stagnation point on the rear face of the bus, B_S is the free stagnation point, D is the saddle point and F1 and F2 are foci of the upper and lower vortices, respectively. b) upper-edge thin vortex B. c) lower-edge thin vortex B.

Figures 10 and 11 sketch the time-averaged flow pattern and the critical points from Figs. 6 and 7 and Figs. 8 and 9 in the two planes of the bus ($z = 0$ and $y = 0$).

According to Hunt *et al.* [10], there can only be a certain number of saddle points for a given number of nodes. They derived a relation for a two-dimensional section of the flow

$$\left(\sum_N + \frac{1}{2}\sum_{N'}\right) - \left(\sum_S + \frac{1}{2}\sum_{S'}\right) = 1 - n \tag{1}$$

where $\sum_N$ is the number of nodes and foci, $\sum_{N'}$ is the number of half-nodes (nodes on the boundaries), $\sum_S$ is the number of saddles and $\sum_{S'}$ is the number of half-saddles. n is the connectedness of the surface. For a singly connected region with no body, $n = 1$; with one body (as in our case) $n = 2$ etc.

Let us now investigate whether the critical points in Figs. 10 and 11 satisfy the topological constraint in Eq. 1. In Fig. 10 $\sum_N = 5$, $\sum_{N'} = 0$, $\sum_S = 1$ and $\sum_{S'} = 10$ so that $(\sum_N + 1/2\sum_{N'}) - (\sum_S + 1/2\sum_{S'}) = 5 - (1 + 5) = -1$ and in Fig. 11 $\sum_N = 6$, $\sum_{N'} = 0$, $\sum_S = 1$ and $\sum_{S'} = 12$ so that $(\sum_N + 1/2\sum_{N'}) - (\sum_S + 1/2\sum_{S'}) = 6 - (1 + 6) = -1$. This agrees with Eq. 1, since $n = 2$. Thus these figures represent a flow that is kinematically possible.

This study was based on the topological and kinematical results of our LES in [11, 12]. For additional details on the flow features and the mechanisms of their origin, we refer to [11, 12].

4 Numerical accuracy

To establish the results' grid independence, two additional computations on different (coarser) grids were made. The near-wall resolution of these grids was $\langle \Delta s^+ \rangle_t = 15 - 580$, $\langle \Delta n^+ \rangle_t = 0.8 - 1.2$ and $\langle \Delta l^+ \rangle_t = 14 - 217$ and $\langle \Delta s^+ \rangle_t = 15 - 580$, $\langle \Delta n^+ \rangle_t = 11.8 - 18.8$ and $\langle \Delta l^+ \rangle_t = 14 - 217$ for the medium and the coarse grids, respectively. Results for the global topological quantities, the forces and the velocities between the three simulations and the experiments (if available) were compared.

There is a 24% difference in re-attachment lengths X_{R1} and X_S between the fine and medium-grid simulations (Table 1). The corresponding difference in the re-attachment length, X_r, measured at $y = 0$ was 20%, but the difference in the position of the free stagnation point, X_{free}, was only 9%. The value of X_r from the coarse-grid simulation differed by only 1% from the medium-grid value (Table 1). There is a 6% difference in the time-averaged drag coefficient $\langle C_D \rangle_t$ between the fine and the medium-grid simulations and a 54% difference between the medium and the coarse-grid simulations (see Table 2). The great difference in $\langle C_D \rangle_t$ between the medium and the coarse-grid simulations is caused by the failure of the coarse-grid simulation to predict

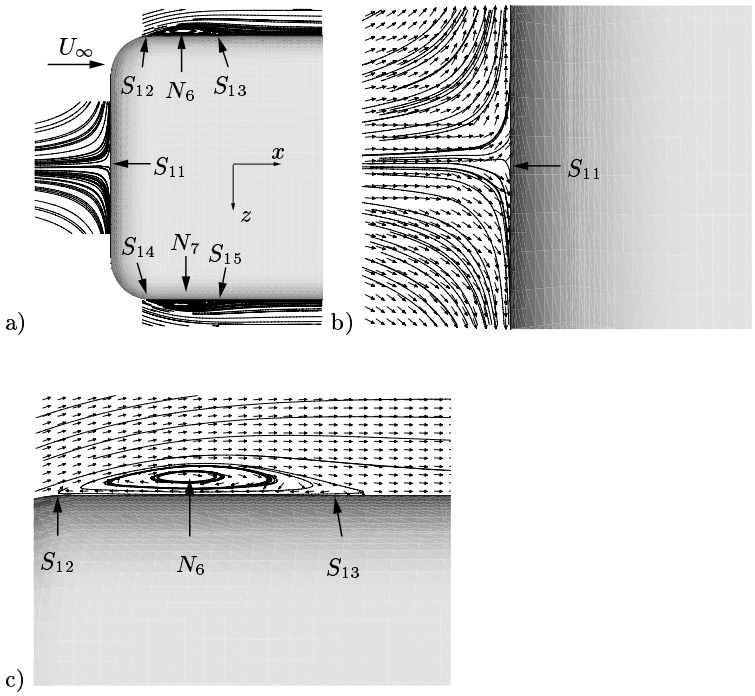

Fig. 8. a) Time-averaged streamlines projected onto plane $y = 0$ showing half-saddles S_{11}-S_{15} and foci N_6 and N_7. b) Zoom of the stagnation point (half-saddle S_{11}). c) Zoom of the lateral side vortex.

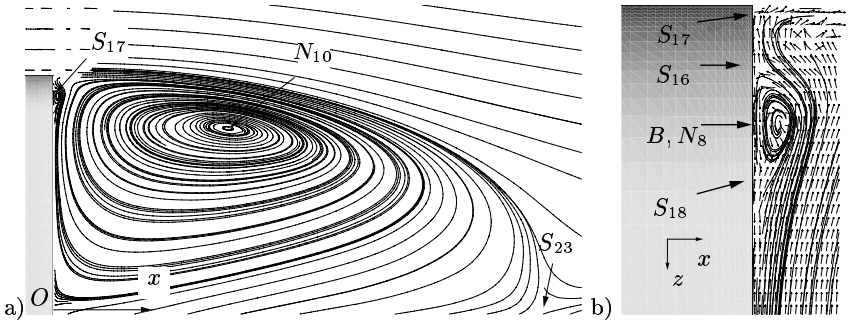

Fig. 9. a) Time-averaged streamlines projected onto plane $y = 0$. N_{10} is foci and S_{23} is saddle point. b) Zoom of the lateral-edge thin vortex, B, for $z > 0$. S_{16}-S_{18} are half-saddles and N_8 is focus.

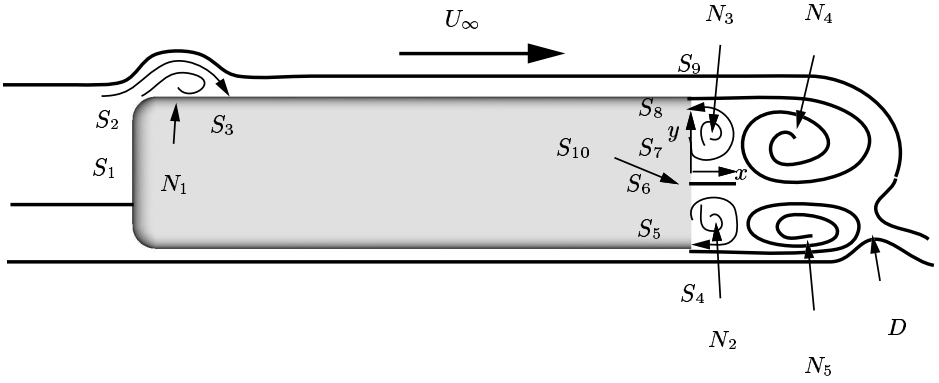

Fig. 10. Schematic representation of time-averaged streamlines and singular points on the symmetry plane, $z = 0$, of the bus. S_1-S_{10} are half-saddles, N_1-N_5 are foci and D is the saddle point.

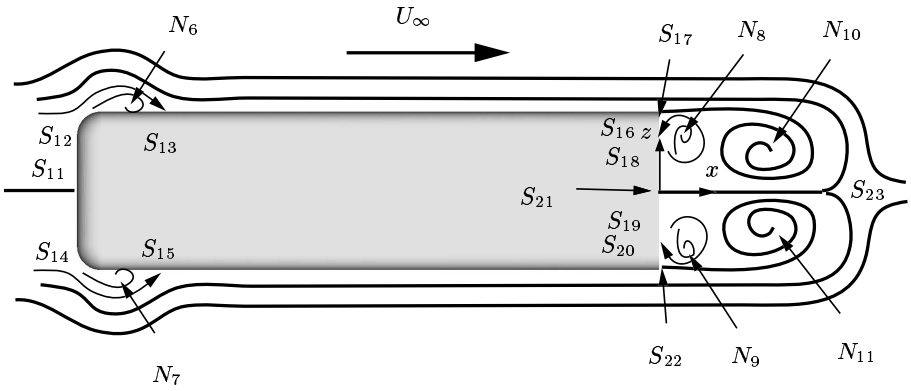

Fig. 11. Schematic representation of time-averaged streamlines and singular points on the plane $y = 0$. S_{11}-S_{22} are half-saddles, N_6-N_{11} are foci and S_{23} is the saddle point.

separation regions R and L in Fig. 2, thus producing too low a surface pressure at the front edges of the body. The time-averaged lift coefficient $\langle C_L \rangle_t$ remained unchanged between the coarse and medium-grid simulations and decreased by some 6% from the medium to the fine-grid simulations. The time-averaged pressure coefficient at the rear face of the body $\langle C_p \rangle_t$ changed by $3-4\%$ with different spatial resolutions (Table 2). Unfortunately, the drag and the lift coefficients were not measured in the experiments.

The velocity profiles changed most in the wake region (Fig. 12), but the trend is consistent with grid refinement. Although the shapes of the computed velocity profiles in the separation bubble ($x/H = 0.32$ and $x/H = 0.98$) are similar to those of the experiments, there are some differences in the core of

the bubble (Fig. 12). The agreement of the experimental data inside the separation bubble with LES results becomes worse with grid refinement (Fig. 12). To explain this behavior we computed the r.m.s. velocity intensity in the separation bubble and found that these were locally higher than 55% of the time-averaged velocity. Duell and George [7, 8] used hot-wire anemometry for velocity measurements. They found [8] that these intensities varied between 32% and 70%. According to Chandrsuda and Brashaw [4], the hot-wire measurements are reliable only if the r.m.s. velocity intensity is less than about 30%. Chandrsuda and Brashaw [4] also found that, when the turbulence intensity exceeds 50%, hot-wire results become highly unreliable. From this we conclude that the experimental data are not accurate in this region. Position $x/H = 1.63$ is downstream of the separation bubble, but the local turbulence intensity is still in excess by some 30% of the time-averaged velocity. Figure 12 shows that, at $x/H = 1.63$, agreement between computed and measured profiles becomes better with better spatial resolution.

Contribution	X_{R1}/H	X_S/H	X_r/H	X_{free}/H	Y_{free}/H
Duell and George [8]	-	-	1.1	-	-
coarse	0	0	1.44	1.6	−0.17
medium	0.41	0.41	1.42	1.42	−0.23
fine	0.33	0.33	1.18	1.3	−0.2

Table 1. Lengths for re-attachment on the roof (X_{R1}), lateral walls (X_S) and behind the bus (X_r). X_{free} and Y_{free} are coordinates of the free stagnation point at the closure of the separation bubble.

Case	$\langle C_D \rangle_t$	$\langle C_L \rangle_t$	$\langle \overline{C}_p \rangle_t$	St_p
coarse	0.206	-0.066	-0.216	0.073
medium	0.318	-0.066	-0.224	0.055
fine	0.33	-0.071	-0.229	0.059

Table 2. Time-averaged pressure drag, lift and rear pressure coefficients and dominating frequency (St_p) of the $\overline{C}_p$ signal (note that $\overline{C}_p$ means the integrated C_p over the rear surface).

5 Conclusions

The dense data obtained in LES is suited for delicate topological studies of the flow. The critical points and the bifurcation lines on the surface of the vehicle

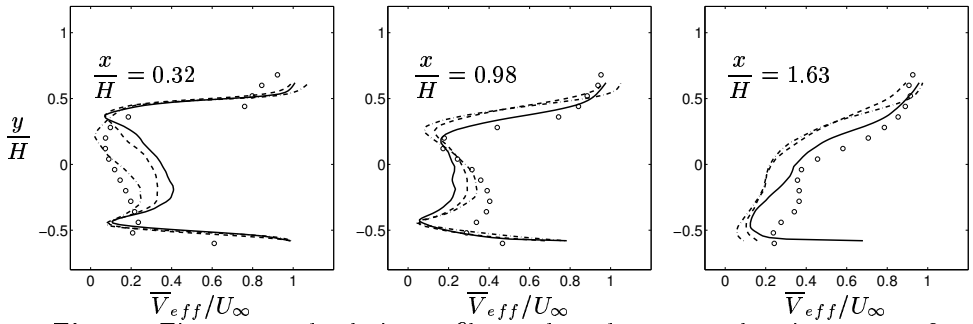

Fig. 12. Time-averaged velocity profiles at three downstream locations at $z = 0$. Fine grid (solid curve); medium grid (dashed curve); coarse grid (dashed-dotted curve); experiment (symbols).

can be displayed and provide the information on the motion of the near-surface fluid particles. This paper demonstrates such use of LES data to create a topological picture of the external vehicle flow (i.e. flow around a simplified bus). The singular points were not only identified but also classified according to their stability (stable and unstable) and their influence on the surrounding fluid (nodes, foci and saddles). A similar distinction was made between the negative and positive bifurcation lines in this flow. In addition to these studies, a relation between the number of nodes and the number of saddles was used to determine whether the simulation produced a kinematically possible flow. This analysis may be useful when poor resolution prevents determination of the character of a solitary singular point. Classifying the remaining points in topological terms as nodes and saddles and using a relation between their number, the nature of the last point can be determined.

References

[1] S. R. Ahmed, G. Ramm, and G. Faltin. Some salient features of the time averaged ground vehicle wake. SAE Paper 840300, 1984.

[2] J. Barlow, R. Guterres, R. Ranzenbach, and J. Williams. Wake structures of rectangular bodies with radiused edges near a plane surface. SAE Paper 1999-01-0648, 1999.

[3] P. W. Bearman, J. P. Davis, and J. K. Harvey. Measurement of the structure of road vehicle wakes. *International Journal of Vehicle Design,Technological Advances in Vehicle Design Series, SP3, Impact of Aerodynamics on Vehicle Design*, pages 493–499, 1983.

[4] C. Chandrsuda and P. Bradshaw. Turbulence structures of reattaching mixing layer. *Journal of Fluid Mechanics*, 110:171–194, 1981.

[5] S. Dahlström and L. Davidson. Hybrid RANS-LES with additional conditions at the matching region. In *4th Int. Symp. on Turbulence Heat and Mass Transfer*, Antalya, Turkey, 2003.

[6] L. Davidson and S.-H. Peng. A hybrid LES–RANS model based on a one-equation SGS model and a two-equation $k-\omega$ model. In E. Lindborg, A. Johansson, J. Eaton, J. Humphrey, N. Kasagi, M. Leschziner, and M. Sommerfeld, editors, *The Second International Symp. on Turbulence and Shear Flow Phenomena*, volume 2, pages 175–180, Stockholm, 2001.

[7] E. G. Duell. *Experimental investigation of unsteady near wakes of ground vehicle bodies*. PhD thesis, Cornell University, 1994.

[8] E. G. Duell and A. R. George. Experimental study of a ground vehicle body unsteady near wake. SAE Paper 1999-01-0812, 1999.

[9] T. Han. Computational analysis of three-dimensional turbulent flow around a bluff body in ground proximity. *AIAA Journal*, 27(9):1213–1219, 1989.

[10] J. C. R. Hunt, C. J. Abell, J. A. Peterka, and H. Woo. Kinematical studies of the flows around free or surface-mounted obstacles; applying topology to flow visualization. *Journal of Fluid Mechanics*, 86:179–200, 1978.

[11] S. Krajnović. *Large Eddy Simulations for Computing the Flow Around Vehicles*. PhD thesis, Dept. of Thermo and Fluid Dynamics, Chalmers University of Technology, Gothenburg, 2002.

[12] S. Krajnović and L. Davidson. Numerical Study of the Flow Around the Bus-Shaped Body. *ASME: Journal of Fluids Engineering*, 125:500–509, 2003.

[13] A. E. Perry and M. S. Chong. A description of eddying motions and flow patterns using critical-point concepts. *Ann. Rev. Fluid Mech.*, 19:125–155, 1987.

[14] J. Smagorinsky. General circulation experiments with the primitive equations. *Monthly Weather Review*, 91(3):99–165, 1963.

[15] P. R. Spalart, W. H. Jou, M. Strelets, and S. R. Allmaras. Detached-eddy simulation of an airfoil at high angle of attack. In *Advances in DNS/LES, Proceedings of the First AFOSR International Conference on DNS/LES*, 1997.